UV Absorption by TiO_2 Films in Photocatalytic Reactors: Effect of Fold Curvature

Adam A. Donaldson and Zisheng Zhang
Dept. of Chemical and Biological Engineering, University of Ottawa, 161 Louis Pasteur Street, Ottawa, Canada K1N 6N5

DOI 10.1002/aic.12683
Published online June 14, 2011 in Wiley Online Library (wileyonlinelibrary.com).

Corrugated reactors are known for their use in applications requiring exposure of a reaction medium or catalyst to UV radiation. During manufacture, the idealized sharp corner of a V-shaped geometry is replaced with a fold having quantifiable curvature. The effects of this curvature on UV absorption patterns, spatial absorption/incidence patterns and the total absorption efficiency are explored for a broad range of fold curvatures and film angles using a conservative, finite-element based discrete-ordinate model. The presence of curvature was found to redistribute radiation from the deepest confines of the V-shaped geometry to surfaces closer to the light source. The simulations performed suggest that at small film angles, moderate curvature can be incorporated within the fold of the film without significantly affecting the overall absorption efficiency. Detailed absorption data is included for use as a boundary condition for computational fluid dynamics-based simulations linking UV-radiation, reaction kinetics, and mass transfer. © 2011 American Institute of Chemical Engineers *AIChE J,* 58: 1578–1587, 2012
Keywords: photochemical reactions, reactor analysis, computational fluid dynamics, surface chemistry/physics, environmental engineering

Introduction

Ultraviolet radiation-based photodegradation, photosynthesis, photolysis, and photocatalytic reactions involving both gases and liquids have long been considered for applications in water treatment and clean technologies,[1-6] with recent interests in areas of food preservation[7-9] and methanol production.[10-13] Many of these processes involve the photo-excitation of either a reactant or catalyst as a limiting step governing reaction kinetics, requiring detailed knowledge of the UV absorption profiles within a given reactor geometry to accurately simulate and design optimum configurations.

Radiative transfer in absorbing, reacting, and scattering reaction media has been properly described by a set of integral-differential equations,[14] commonly solved with one of three numerical frameworks: Monte Carlo (MC) approaches[15,16]; discrete ordinate (DO) models[17,18]; and a conservative finite-volume (FV) variant of the DO model.[19,20] These models have been used to determine radiation fields in pseudo homogeneous photoreactors, expressed as the local volumetric rate of energy absorption (LVREA) within regions of the reactor bulk.[21,22] For the case of reactions performed on immobilized catalyst films, the local area-specific rate of energy absorption (LASREA)[23] is more appropriate to describe the absorbed radiation and associated kinetics at the film's surface.

The computational requirements of MC, DO, and FV models often necessitates simplifying assumptions: complex geometries are reduced to 1D or 2D problems; reflections from nonemitting surfaces are simplified or ignored; absorption and extinction properties are averaged across the wavelength spectrum of an emitting source; and for reactions performed on an immobilized film, the reactor medium is

Additional Supporting Information may be found in the online version of this article.

Correspondence concerning this article should be addressed to Z. Zhang at jason.zhang@uottawa.ca.

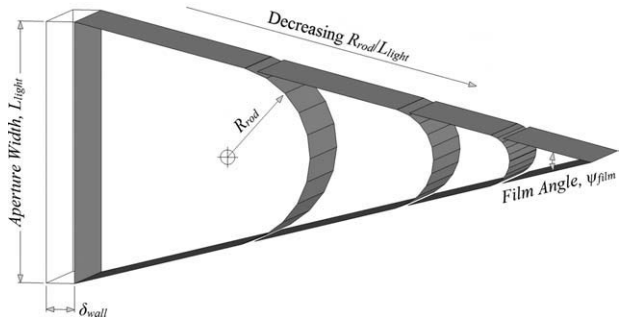

Figure 1. Cross-sectional profiles and characteristic parameters of a V-shaped corrugation with differing R_{rod}/L_{light} ratios.

commonly assumed to have negligible effects on radiation. FV models are often coupled with CFD simulations to correlate radiation absorption, reaction kinetics, mass transfer, and fluid flow for pseudo homogeneous photoreactors.[20] The simultaneous solution of mass, momentum and radiation transfer equations forces equivalency of the time-scale of photon transport, potentially leading to poor descriptions of complex reflections and the LVREA in mediums having spatially (and thus temporally) dependent absorption/transmission properties. For the case of reactions performed on an immobilized film, it is more convenient to decouple radiation transport from fluid flow; solving for the LASREA on the catalyst surface and implementing the resulting absorption profile as a boundary condition in CFD simulations.

In this work, a conservative finite element-based DO method is developed to characterize the radiation absorption profiles on the surfaces of TiO_2 films in a corrugated-plate photocatalytic reactor based on the principles of geometric optics, the absorption and reflection characteristics of the catalyst film, and the refraction properties of the reaction medium and reactor components. This method is used to explore the impact of curvature introduced in the folds of a V-shaped corrugated-plate during manufacturing on the LASREA and absorption efficiency relative to incidence from the light source: accounting for effects of the radiation source, photon recapture through multiple reflections, and the catalyst film angle.

Equipment and Materials

Consider a single corrugation from a conventional corrugated-plate photocatalytic reactor,[23] whose cross-sectional profile can be defined by three parameters (Figure 1): the width of the aperture facing the light source, L_{light}; the angle of the corrugated plate, ψ_{film}; and the equivalent radius of curvature within the fold of the film introduced during manufacturing, R_{rod}. For the current simulations, L_{light} was kept constant at 1 m while ψ_{film} and R_{rod}/L_{light} were varied to numerically examine their effects on the LASREA and UV-A absorption efficiency. Through the use of dimensional similitude, the employed array of geometric configurations is representative of a broad spectrum of triangle-shaped channels encountered in conventional corrugated-plate reactors.

Properties for the acrylic reactor wall were based on those of a fluorescent lamp sleeve: an ultraviolet-light (UV)-transmitting Plexiglas (G-UVT) sheet with thickness of $\delta_{wall} = 0.00635$ m. Two types of radiation sources were considered: a uniform diffuse 120 $W{\cdot}m^{-2}$ UV-A source with emission characteristics similar to a Philips TLK 40W/10R lamp[24]; and solar UV radiation with parallel and diffuse components.

Assumptions

The following assumptions were made in developing and applying the radiation model:

1. Photons from the lamps fall incident on the reactor wall in a diffuse way. This assumption should be close to the real situation, since diffuse emission models have also been found to be suitable for modeling fluorescent lamps.[25] The total irradiance on the surface of the reactor wall was assumed to be 120 $W{\cdot}m^{-2}$, based on measurements in experimental systems.[26]

2. In the UV-A range, solar UV possesses an irradiance with a direct parallel portion of 20 $W{\cdot}m^{-2}$ and a diffuse portion of 10 $W{\cdot}m^{-2}$, consistent with the UV spectrum for low values of the solar zenith angle. The spectral irradiance increases linearly with the wavelength, being zero at 300 nm and reaching a maximum at 390 nm.[27-29] In the modeling reported here, the sun's rays are assumed to be normal to the surface of the reactor wall.

3. The transmittance loss in the acrylic reactor wall is due entirely to extinction in the solid material, where the extinction coefficient, k_{wall} [m^{-1}], can be expressed as:[23]

$$k_{wall} = 88.873 - 66.758 * \tanh\left(\frac{\lambda - 302}{14.684}\right) \quad (1)$$

4. Photons are considered lost once they are reflected back to the acrylic wall from the catalyst film.

5. Photons hitting the TiO_2 film will be subject to either coherent reflection in a diffuse way or absorption. This should be a reasonable approximation since the immobilized catalyst film was found to be opaque to UV-A and optically rough.[26]

6. The dimensionless fraction of incident energy absorbed by the TiO_2 film, $a(\lambda)$, was comparable to that of Zhang et al.,[23,30] which can be numerically expressed as:

$$a(\lambda) = 0.5 - 0.5\tanh\left(\frac{\lambda - 355.66}{12.743}\right) \quad (2)$$

7. Within the UV-A range, the refractive index of the acrylic reactor wall was assumed to be constant at $n_w = 1.49$, based on relevant information from the literature.[31] The reaction medium was assumed to have a refractive index of $n_m = 1.33$, the same as that of water. The reaction medium was assumed to not significantly absorb in the wavelengths of interest.

Computational Methodology

Element construction and discretization

The computational domains were constructed in three stages to allow for versatility in the geometric configuration. The

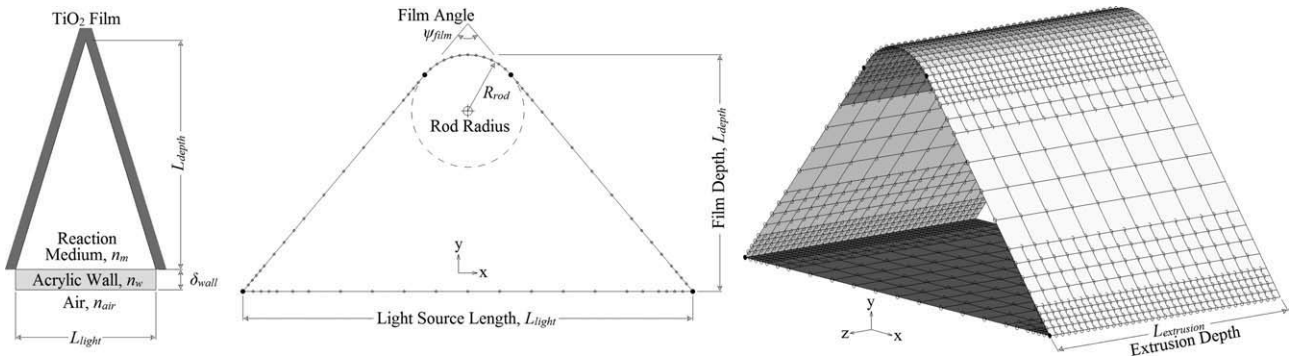

Figure 2. Film reactor conceptualization (left), XY profile (centre) and extruded computational elements (right).

Profile and elements are for $L_{light} = 1$, $R_{rod} = 0.125$, $\psi_{film} = 40°$, and a sample discretization showing three levels of mesh refinement.

cross-sectional profile of the film was first defined in the *XY* plane as a series of lines and arcs, with the interior acrylic reactor wall (i.e., light source) located along the *X*-axis to simplify treatment of the parallel component of solar radiation. An automated mesh refinement algorithm was then applied based on a maximum allowable emission angle, breaking the lines and arcs into a series of linear elements (Figure 2). This discretized profile was then extruded along the *Z*-axis to form the surface elements used to model UV absorption by the TiO_2 films; where the extrusion depth, $L_{extrusion}$, was set to 125% of the maximum diffusive radiation pattern width:

$$L_{extrusion} = 2.5 \tan(\arcsin(n_{air}/n_m))L_{depth} \tag{3}$$

Where L_{depth} is the distance between the acrylic reactor wall and the deepest point within the film fold.

The surface elements were classified as either emitting (light) or diffuse reflecting (film), defined such that the unit normal vector of each was oriented towards the interior of the computational domain. The LASREA incidence for each diffuse reflecting element (i.e., exposure to UV-A radiation in Watts per m^2 receiving surface area, accounting for reflections) was then determined iteratively.

Model equations

Derivation of the expressions for spectral specific irradiance at the sleeve/reaction medium interface for uniform lamp, I_{lamp}, and solar, I_{solar}, light source are described in detail elsewhere.[23] Accounting for refractory effects across the lamp sleeve for an infinite diffuse light source, the diffuse component of spectral specific irradiance for a given light element, *j*, in the computational domain can be expressed as:

$$I_{diff,j}(\lambda,\psi_w) = \begin{cases} W_{diff}\left(\frac{n_m}{n_{air}}\right)^2 \exp\left(-k_{wall}\delta_{wall}\left[1-\left(\frac{n_m}{n_w}\sin\left(\psi_{i,j}\right)\right)^2\right]^{-0.5}\right) & \text{for} \left|\sin(\psi_{i,j})\right| < \frac{n_m}{n_w} \\ 0 & \text{for} \left|\sin(\psi_{i,j})\right| \geq \frac{n_m}{n_w} \end{cases} \tag{4}$$

where δ_{wall} is the thickness of the acrylic reactor wall; $\psi_{i,j}$ is the angle between the unit normal of the current emitting element and the vector between the centers of the emitting element and the receiving element; and W_{diff} is either the spectral irradiance on the surface of the lamp sleeve for a 120 W power source, W_{lamp}, or the spectral irradiance of the diffuse solar UV light source, W_{solar}:

$$W_{lamp}(\lambda) = \frac{(120 \text{ Watts})}{15.75\sqrt{2\pi}} \exp\left(-\frac{(\lambda-353)^2}{2(15.75)^2}\right) \tag{5}$$

$$W_{solar}(\lambda) = (10 \text{ Watts}) \frac{2(\lambda-300)}{(390-300)^2} \tag{6}$$

While W_{solar} is based on a linear increase in incidence with wavelength (assumption 2), W_{lamp} was determined from a normal distribution fit of the emission spectrum of a Philips TLK 40W/10R lamp,[24] scaled to 120W. For a solar light source element, an additional contribution from parallel UV radiation is required, I_{par}, dependent on the angle between the receiving element and the light plane, $\psi_{axis,i}$.

$$I_{par}(\lambda) = (20 \text{ Watts}) \frac{2(\lambda-300)}{(390-300)^2} \exp(-k_{wall}\delta_{wall}) \cos\psi_{axis,i} \tag{7}$$

Note that for light elements located on the XZ geometric plane, $\cos\psi_{axis,i} = n_i \cdot (0\ -1\ 0)$, where n_i is the unit normal vector of the receiving element.

The spectral LASREA incidence on any surface element of the film, $I_i(\lambda)$, can be determined through the summation of irradiance from light elements and reflections from other film elements:

$$I_i(\lambda) = \frac{1}{dA_i}\left[\sum_j^{film}(1-a(\lambda))F_{i,j}I_j(\lambda)dA_j + \sum_j^{light} F_{i,j}I_{diff,j}(\lambda)dA_j\right] + I_{par}(\lambda)^{(solar\ only)} \tag{8}$$

where $a(\lambda)$ is the absorbance of the TiO_2 film at the specified wavelength, λ; dA_i and dA_j are the surface areas of elements *i* and *j*; and $F_{i,j}$ is an emission factor determined from solid angles, $SA_{i,j}$, and Lambert's cosine law:

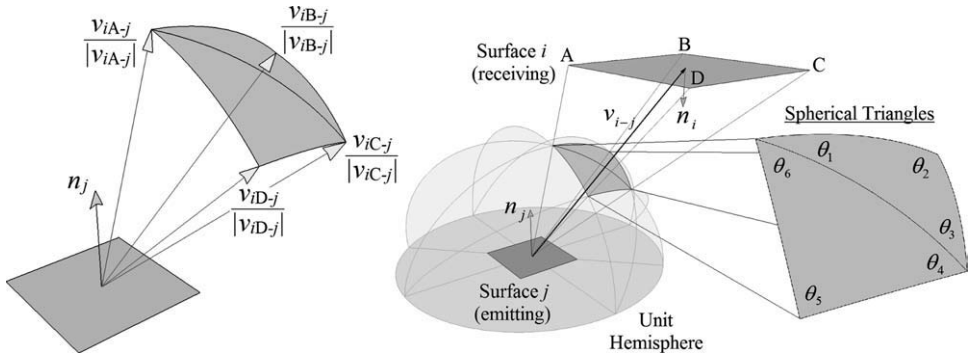

Figure 3. Visualization of methodology used to determine the solid angle of a receiving element, *i*, for an emitting surface, *j*.

$$F_{i,j} = \frac{SA_{i,j}}{\pi}\cos\left(\psi_{i,j}\right) = \frac{SA_{i,j}}{\pi}\frac{\left(n_j \cdot v_{i-j}\right)}{\left|v_{i-j}\right|} \tag{9}$$

Note that n_j is the unit normal vector of the emitting element surface, while $v_{i\text{-}j}$ is the vector between the centres of the emitting and receiving elements (Figure 3).

In previous literature, the solid angle is commonly approximated as the projected area of the receiving element on a unit hemisphere around the emitting surface:

$$SA_{i,j} = \frac{-\left(n_i \cdot v_{i-j}\right)dA_i}{\left|v_{i-j}\right|^3} \tag{10}$$

However, this approximation is only valid when the calculated solid angle is very small; rapidly degrading as the distance between the two surfaces decreases. For a V-shaped film having sharp corners within the computational domain, Eq. 10 leads to the development of numerical instability in the corner elements regardless of the level of mesh refinement used. For this reason, the solid angle was determined from spherical triangles[32] formed by unit vectors between the centre of the emitting element and the corners of the receiving element (Figure 3):

$$SA_{i,j} = -2\pi + \sum_{k=1\rightarrow 6}\theta_k \tag{11}$$

$$\theta_1 = \frac{\arccos(\cos[\angle BjC] - \cos[\angle AjB]\cos[\angle AjC])}{\sin[\angle AjB]\sin[\angle AjC]} \tag{12a}$$

$$\theta_2 = \frac{\arccos(\cos[\angle AjC] - \cos[\angle AjB]\cos[\angle BjC])}{\sin[\angle AjB]\sin[\angle BjC]} \tag{12b}$$

$$\theta_3 = \frac{\arccos(\cos[\angle AjB] - \cos[\angle AjC]\cos[\angle BjC])}{\sin[\angle AjC]\sin[\angle BjC]} \tag{12c}$$

$$\theta_4 = \frac{\arccos(\cos[\angle AjD] - \cos[\angle CjD]\cos[\angle AjC])}{\sin[\angle CjD]\sin[\angle AjC]} \tag{12d}$$

$$\theta_5 = \frac{\arccos(\cos[\angle AjC] - \cos[\angle AjD]\cos[\angle CjD])}{\sin[\angle AjD]\sin[\angle CjD]} \tag{12e}$$

$$\theta_6 = \frac{\arccos(\cos[\angle CjD] - \cos[\angle AjC]\cos[\angle AjD])}{\sin[\angle AjC]\sin[\angle AjD]} \tag{12f}$$

where the angles in Eqs. 12a–f are determined from $v_{iA\text{-}j}$, $v_{iB\text{-}j}$, $v_{iC\text{-}j,}$ and $v_{iD\text{-}j}$ (Figure 3):

$$\cos[\angle AjB] = \frac{v_{iA-j} \cdot v_{iB-j}}{\left|v_{iA-j}\right|\left|v_{iB-j}\right|} \tag{13}$$

General solution procedure

Following mesh generation, the spectral LASREA incidence was determined for each film element based solely on the emissions from light sources. Neglecting the first summation in Eq. 8, the resulting $I_i(\lambda)$ represents the incidence with no reflection of photons. The neglected summation term was then solved iteratively for all film elements until the variation between iterations was negligible, where each iteration accounted for an additional reflection of the photons striking the surface of the film. An overview of the general solution procedure is provided in Figure 4.

Simulation Results and Discussion

Figures 5–12 illustrate the calculated typical radiation fields and absorption efficiencies on the TiO_2-coated corrugated plates at the center of the extruded length, where end effects were found to be insignificant. The dimensionless position on the corrugated plate cross-section, X/L_{light}, varies along the x-axis in Figure 2, where the corresponding depth at any given point is a function of the film angle and $R_{\text{rod}}/L_{\text{light}}$. The incidence in these figures refers to the LASREA incidence determined from Eqn. (8) when photon-reflection is ignored. Absorption, no recapture refers to the LASREA absorption if no reflected photon could be captured, while the LASREA accounts for the effect of recapturing reflected photons on energy absorption.

Spectral radiation patterns

Typical radiation fields for lamp-illuminated corrugated plates are plotted in Figure 5 for a 20° film angle and $R_{\text{rod}}/L_{\text{light}} = 0$ (V-shaped) and 0.125. While the radiation field near the light source ($X/L_{\text{light}} = 0$) remained comparable for both geometries, the presence of curvature within the fold of the film ($X/L_{\text{light}} \sim 0.5$) resulted in a significant increase in magnitude of incidence, absorption no recapture and LASREA across all wavelengths for $R_{\text{rod}}/L_{\text{light}} = 0.125$. This increase is primarily attributed to the directional orientation of the receiving surfaces within the fold, whereby the solid angle increases as the receiving surface's orientation

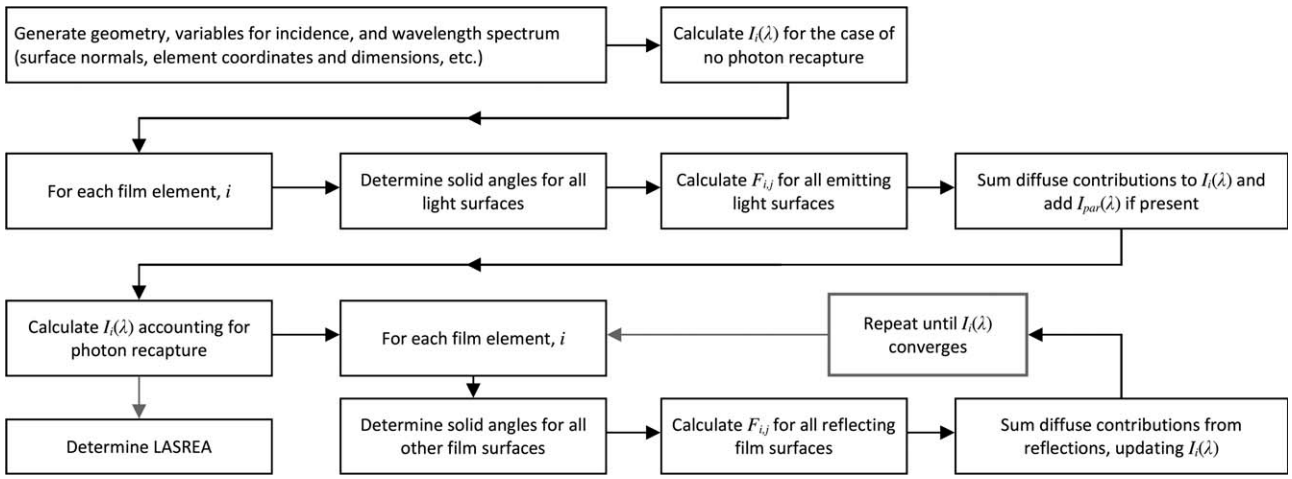

Figure 4. General solution procedure to determine $I_i(\lambda)$ for elements within a given geometry.

becomes parallel to that of the light source (i.e., direct exposure), leading to significantly increased incidence, and subsequently, absorption. However, as discussed later, the parallel orientation also reduces the overall efficiency since photons are primarily reflected back to the light aperture where they are considered lost. Similar results were observed for solar-illuminated corrugated plates with equivalent geometric configurations (Figure 6). The reduced UV absorbance of the TiO_2 film at higher wavelengths is clearly illustrated by the solar-lit spectral distributions, in that both the absorption no recapture and LASREA drop off quickly at higher wavelengths despite the increased incidence. The LASREA at intermediate wavelengths is higher than that of the absorption no recapture within the fold of the geometries ($X/L_{\text{light}} \sim 0.5$) due to increased absorption of reflected/scattered UV radiation, consistent with previous literature.[23]

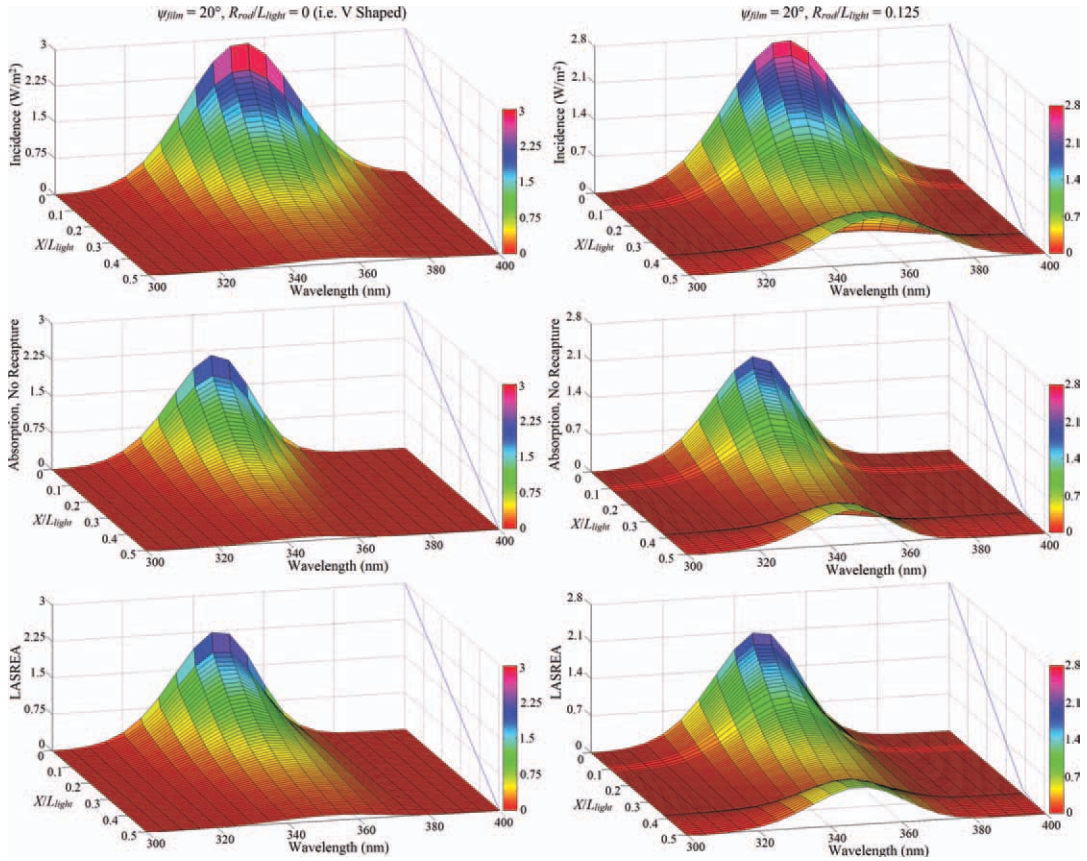

Figure 5. Spectral radiation field on the surface of two lamp-lit geometries (cross-section depicted on *XZ* plane of each figure), where $X = 0$ is closest to the radiation source.

[Color figure can be viewed in the online issue, which is available at wileyonlinelibrary.com].

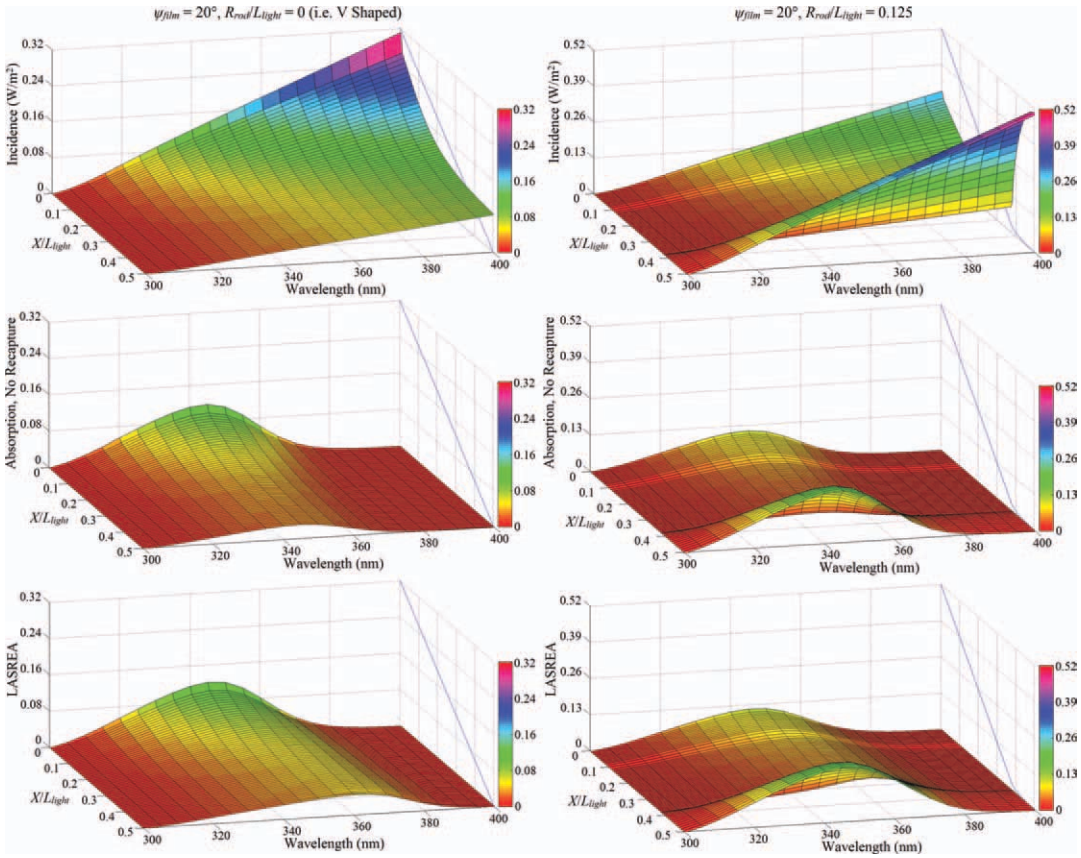

Figure 6. Spectral radiation field on the surface of two solar-lit geometries (cross-section depicted on *XZ* plane of each figure), where $X = 0$ is closest to the radiation source.

[Color figure can be viewed in the online issue, which is available at wileyonlinelibrary.com].

Wavelength-integrated radiation patterns and efficiencies

Comparing the wavelength-integrated energy flux at the surface of the TiO_2 film for lamp-lit, V-shaped and $R_{rod}/L_{light} = 0.125$ geometries of three different film angles (Figure 7), deviations in the radiation profiles are only observed in regions approaching the fold curvature (i.e., $X/L_{light} \sim 0.375$ for $R_{rod}/L_{light} = 0.125$). The parallel component of solar radiation appears to extend this region of deviation to lower values of X/L_{light} (Figure 8), where reflections from the film opposite to the receiving surface significantly increases the incident radiation and resulting LASREA at $X/L_{light} < 0.375$

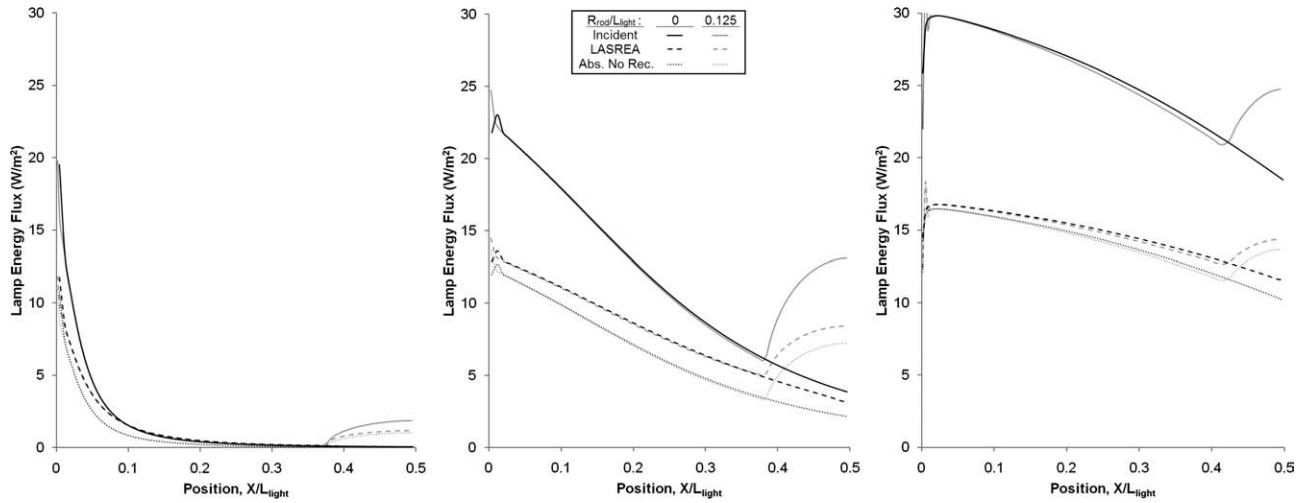

Figure 7. Incidence, LASREA, and absorption with no recapture profiles for lamp-lit geometries with $\psi_{film} = 5^\circ$ (left), 40° (centre), and 100° (right).

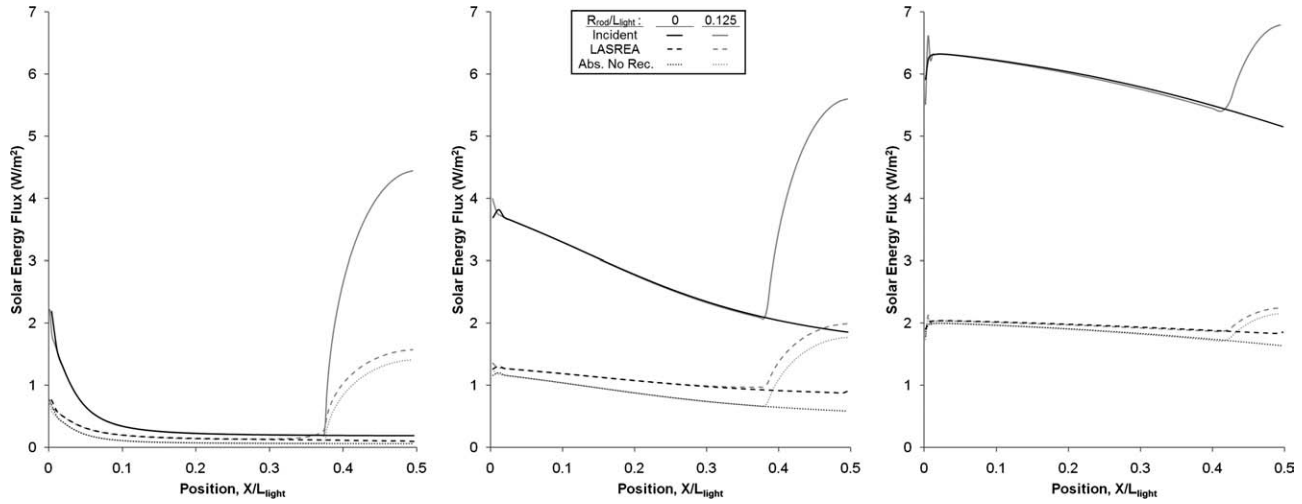

Figure 8. Incidence, LASREA, and absorption with no recapture profiles for solar-lit geometries with ψ_{film} = 5° (left), 40° (center), and 100° (right).

and small film angles (Figure 9). Consistent with previous literature,[23,33,34] the LASREA and absorption no recapture are comparable for high film angles where reflection and recapture of UV radiation is minimal. As the film angle is decreased for the V-shaped geometry, the LASREA gradually approaches the incident energy flux, where the ratio of the LASREA to incidence of a diffuse light source (i.e., lamp-lit) can exceed 1 in localized regions of the geometry (Figure 10). Due to the large component of poorly absorbed, high-wavelength radiation present in the parallel component of the solar light source, the local ratio of LASREA to incidence remained considerably lower than that of a diffuse light source (although still almost twice that of the absorption no recapture for low film angles).

The presence of curvature in the film fold had a dramatic effect on the localized LASREA/incidence ratio approaching and within the region with curvature (Figure 11). At low film angles ($\psi_{film} < 100°$), incident radiation which would normally be reflected and absorbed within the sharp fold of a V-shaped geometry ($X/L_{light} \sim 0.5$) was instead reflected and redistributed along the film surface, concentrated within the $0.2 < X/L_{light} < 0.375$ region for $R_{rod}/L_{light} = 0.125$. The resulting local ratios of LASREA/incidence for both solar and lamp-lit geometries exceeded the theoretical ratio for absorption with no recapture by over 300% at the lowest film angle simulated, with the greatest ratio observed in the region closest to the start of fold curvature. The peaks observed at $X/L_{light} \sim 0.375$ for low film angles (Figure 11) correspond to the geometric focal points of the opposing surfaces for the assumed Lambertian scattering behavior. The LASREA/incidence ratio rapidly decreases as X/L_{light} approached 0.5, where the increasingly parallel orientation of the receiving surface and light source reduced the extent of multiple reflections observed. At higher film angles ($\psi_{film} > 100°$), the presence of fold curvature primarily led to only the later of the two effects described, where the incidence

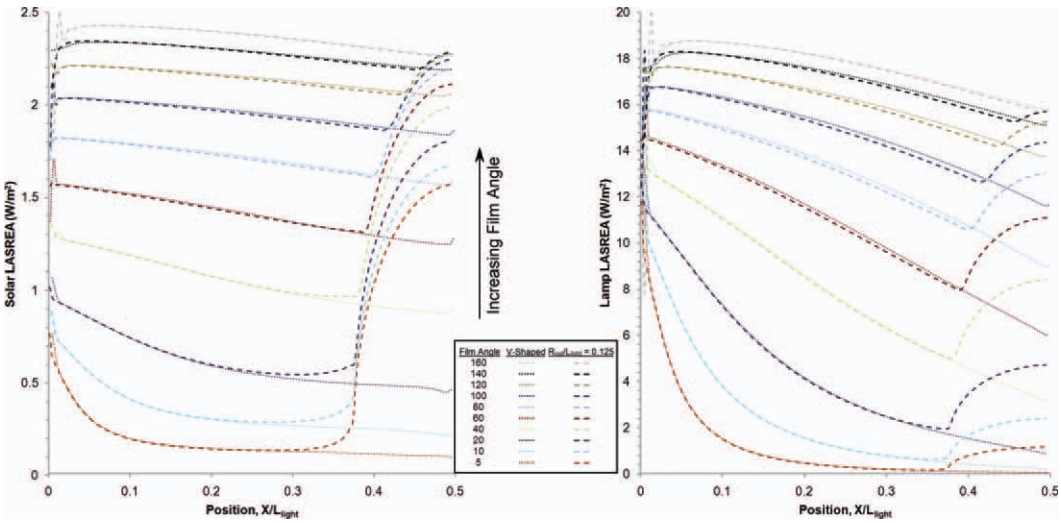

Figure 9. LASREA profiles for solar-lit (left) and lamp-lit (right) geometries for the V-shaped and R_{rod}/L_{light} = 0.125 geometries.

Note that $X = 0$ is closest to the radiation source. [Color figure can be viewed in the online issue, which is available at wileyonlinelibrary.com]

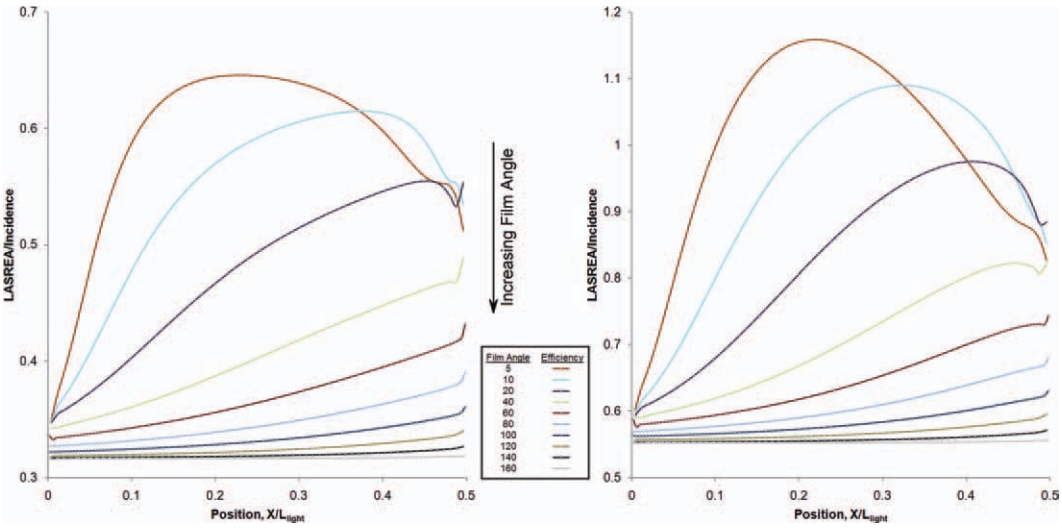

Figure 10. Absorption efficiency profiles for solar-lit (left) and lamp-lit (right) V-shaped geometries, where $X = 0$ is closest to the radiation source.

[Color figure can be viewed in the online issue, which is available at wileyonlinelibrary.com].

increased beyond that observed for a V-shaped geometry (Figures 7 and 8), but with fewer multiple reflections and a lower LASREA/incidence ratio (Figure 10 vs. Figure 11 at equivalent X/L_{light}). Note that the local LASREA/incidence ratios do not account for the variation in *incidence* with X/L_{light}, and thus are not reflective of the overall absorption efficiency of the geometry.

Surface-integrated absorption efficiency

The absorption efficiencies of simulated geometries were determined from the ratio of the surface-integrated LASREA to the surface-integrated incidence (Figure 12). At low film angles, the presence of mild curvature in the film fold (i.e., low values of R_{rod}/L_{light}) has a negligible effect on the overall absorption efficiency, where the incident energy normally absorbed in the sharp fold of a V-shaped geometry is redistributed along the length of the film region. As the film angle increases and the extent of multiple reflections decreases, the absorption efficiency becomes more sensitive to fold curvature. At film angles above 40°, the introduction of fold curvature immediately results in a reduction in overall absorption efficiency for the geometry, until the effect of R_{rod}/L_{light} becomes negligible at $\psi_{film} > 100°$. The variation in efficiencies at $R_{rod}/L_{light} = 0.5$ are primarily the result of the tangential condition used to generate the initial two-dimensional profile (Figure 2), where the straight film length adjacent to the light source and the transition to the curved region varies with ψ_{film}.

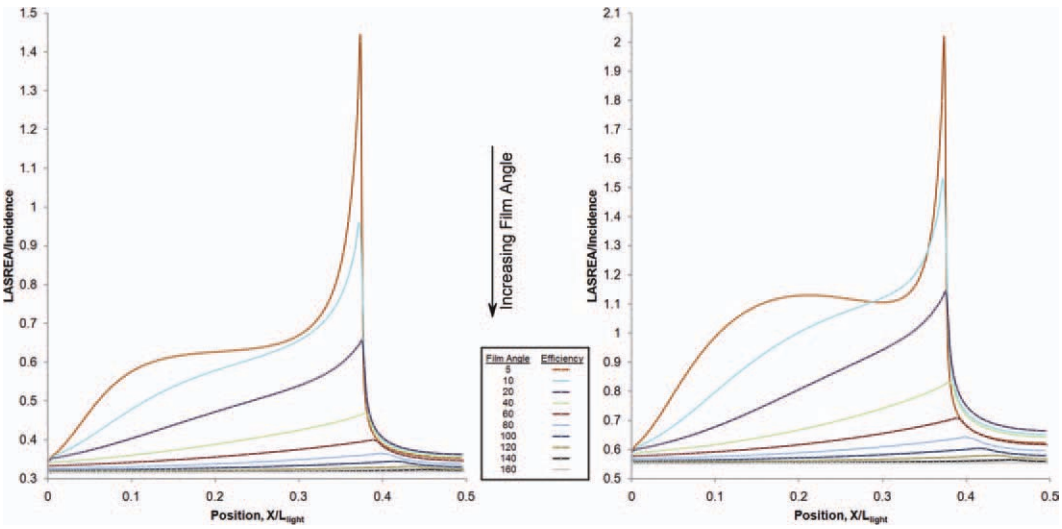

Figure 11. Absorption efficiency profiles for solar-lit (left) and lamp-lit (right) geometries with $R_{rod}/L_{light} = 0.125$, where $X = 0$ is closest to the radiation source.

[Color figure can be viewed in the online issue, which is available at wileyonlinelibrary.com].

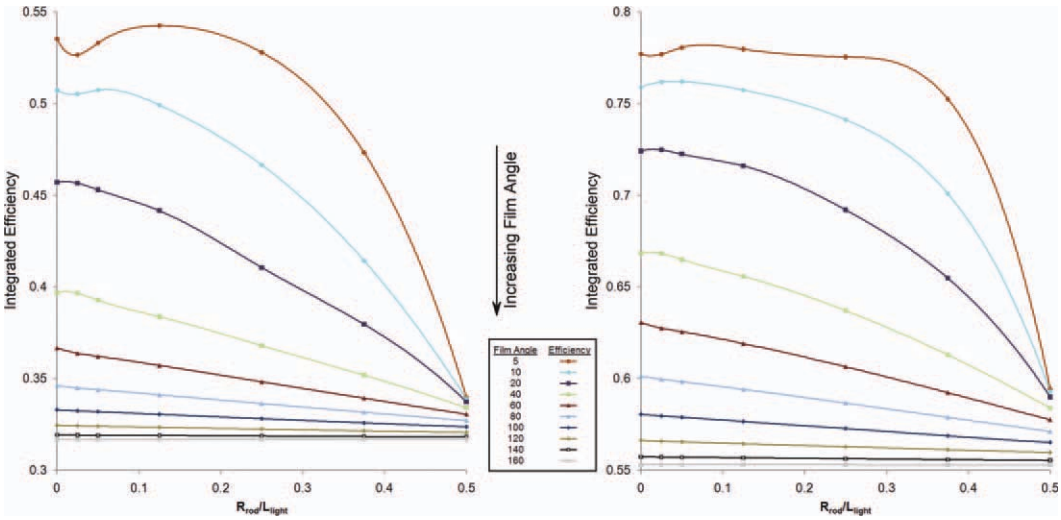

Figure 12. Surface-integrated absorption efficiency at all R_{rod}/L_{light} ratios and film angles for solar-lit (left) and lamp-lit (right) geometries.

[Color figure can be viewed in the online issue, which is available at wileyonlinelibrary.com].

Dimensional similitude of results

While these simulations were completed for a constant $L_{light} = 1$ m, the results obtained can be scaled to similar geometric configurations through dimensional similitude providing the following assumptions are met: the acrylic reactor wall is comparable in width and transmission properties, the absorption coefficient of the film is comparable with that defined in assumption 6, and the fluid properties are comparable with those in assumption 7. A change in the light source power will result in a proportional change in the reported LASREA provided the spectral distribution of diffuse and parallel light sources are consistent with assumptions 1 and 2, and the ratio of parallel to diffuse light power for solar radiation is equivalent (i.e., low solar zenith angle). If all of these conditions are met, the results reported here can be extended to any corrugated photocatalytic reactor design with equivalent ψ_{film} and R_{rod}/L_{light}. Since the application of the simulated LASREA as a boundary condition in simulations of photocatalytic reactors requires knowledge of the spatial distribution of the LASREA,[35,36] tabulated LASREA data for a broad range of film angles and R_{rod}/L_{light} combinations have been included as supplemental electronic data.

Summary and Future Work

The radiation fields on TiO_2-coated corrugated plates were modeled using a conservative DO approach for film angles from 5° to 160° and fold curvatures ranging from the idealized V-shaped ($R_{rod}/L_{light} = 0$) to a semicircular design ($R_{rod}/L_{light} = 0.5$). At low film angles, mild fold curvature introduce during manufacturing had a minimal effect on the overall absorption efficiency, redistributing the incidence from the depths of the fold to regions of the surface closer to the light source. As the film angle increased, insufficient recapture of redistributed UV radiation resulted in efficiency losses with the introduction of curvature. For large film angles ($\psi_{film} > 100°$), the effects of curvature became negligible as the bulk of redirected radiation from the film fold fell incident on the acrylic reactor wall.

The presence of curvature within the fold of the corrugated plate reactor had a significant effect on the LASREA, which must be accounted for when simulating the relative performance of reactor configurations. While the introduction of curvature may result in reduced overall absorption efficiency, most of the energy lost would normally fall incident on the deep confines of the fold where mass-transfer may supersede the LASREA as the limiting step governing reaction kinetics. An efficient reactor design would thus employ the radiation-dependent reaction kinetics at the surface of the film to match the spatial LASREA distribution to the localized mass transfer rate resulting from flow. A generalized analysis of the effects of film angle and fold curvature on localized mass transfer rates near the surface of a TiO_2 film will be the subject of future work, linking the LASREA distributions and flow conditions for orders of reactions commonly found in clean technology. For specific applications, the LASREA data provided in the electronic supplementary material can be applied to a broad range of corrugated plate reactor designs through dimensional similitude, simplifying the modeling process for reaction kinetics and mass transfer in flowing systems.

Notation

$a(\lambda)$ = dimensionless spectral absorption coefficient for the TiO_2 film
dA_i = area of surface i (m^2)
dA_j = area of surface j (m^2)
$F_{i,j}$ = emission factor for surface j emitting to surface i
$I_{diff,j}$ = irradiance of emitting element j due to diffuse light sources (W/m^2)
$I_i(\lambda)$ = local area-specific energy incidence on film surface i (W/m^2)
I_{lamp} = irradiance from a lamp light source (W/m^2)
I_{par} = irradiance from parallel component of solar light source (W/m^2)
I_{solar} = irradiance from a solar light source (W/m^2)

k_{wall} = extinction coefficient of the reactor wall (m^{-1})
L_{depth} = reactor depth (m)
$L_{extrusion}$ = Z-axis extrusion length of the simulated geometry (m)
L_{light} = light aperture width (m)
n_{air} = refractive index of air
n_i = unit normal of receiving element
n_j = unit normal of emitting element
n_m = refractive index of reaction medium (water)
n_w = refractive index of reactor wall (acrylic)
R_{rod} = radius of curvature of the film fold (m)
$SA_{i,j}$ = solid angle between emitting surface j and receiving surface i
v_{i-j} = vector from center of surface j to centre of surface i
W_{diff} = diffuse light source power (W/m^2)
W_{lamp} = lamp light source power (W/m^2)
W_{solar} = solar light source power (W/m^2)
X = X-axis projected position along the reactor film
δ_{wall} = thickness of the acrylic reactor wall (m)
θ_k = angles within spherical triangles on unit-hemisphere of emitting surface
λ = light wavelength (nm)
$\psi_{axis,i}$ = angle between n_i and surface normal of light source
ψ_{film} = angle of the corrugated plate, film angle
$\psi_{i,j}$ = angle between n_j and v_{i-j} connecting vector

Literature Cited

1. Matthews RW. Photooxidation of organic impurities in water using thin films of titanium dioxide. *J Phys Chem*. 1987;91:3328.
2. Aguado MA, Giménez J, Cervera-March S. Continuous photocatalytic treatment of Cr(VI) effluents with semiconductor powders. *Chem Eng Commun*. 1991;104:71.
3. Belhacova L, Krysa J, Jirkovsky J. Inactivation of microorganisms in a flow-through photoreactor with an immobilized TiO_2 layer. *J Chem Technol Biotechnol*. 1999;74:149.
4. Lyn DA, Chiu K, Blatchley ER. Numerical modeling of flow and disinfection in UV disinfection channels. *J Environ Eng*. 1999;125: 17–26.
5. Lawryshyn YA, Cairns B. UV disinfection of water: the need for UV reactor validation. *Water Sci Technol. Water Supply* 2003;3: 293–300.
6. Ducoste JJ, Liu D, Linden K. Alternative approaches to modeling fluence distribution and microbial inactivation in ultraviolet reactors. Lagrangian versus Eulerian. *J Environ Eng*. 2005;10:1393–1403.
7. Kucuk S, Arastoopour H, Koutchma T. Modeling of UV dose distribution in a thin-film UV reactor for processing of apple cider. *J Food Eng*. 2003;65:125–136.
8. Beltran JA, Barbosa-Cánovas, GV. Advantages and limitations on processing foods by UV light. *Food Sci Technol Int*. 2004;10:137–147.
9. Mahmoud NS, Ghaly AE. On-line sterilization of cheese whey using ultraviolet radiation. *Biotechnol Prog*. 2004;20:550–560.
10. Noceti RP, Taylor CE, D'Este JR. Photocatalytic conversion of Methane. *Catal Today* 1997;33:199–204.
11. Taylor CE, Noceti RP. New developments in the photocatalytic conversion of Methane to Methanol. *Catal Today*. 2000;55:259–267.
12. Gondal MA, Hameed A, Suwaiyan A. Photocatalytic conversion of methane into methanol using visible laser. *Appl Catal A: General*. 2003;243:165–174.
13. Gondal MA, Hameed A, Yamani ZH, Arfaj A. Photocatalytic transformation of methane into methanol under UV laser irradiation over WO_3, TiO_2 and NiO catalysts. *Chem Phys Lett*. 2004;392:377.
14. Cassano AE, Martin CA, Brandi RJ, Alfano OM. Photoreactor analysis and design: fundamentals and application. *Ind Eng Chem Res*. 1995;34:2155–2201.
15. Spadoni G, Bandini E, Santarelli F. Scattering effects in photosensitized reactions. *Chem Eng Sci*. 1978;33:517.
16. Yokota T, Cesur S, Suzuki H, Baba H, Takahata Y. Anisotropic cattering model for estimation of light absorption rates in photoreactor with heterogeneous medium. *J Chem Eng*. 1999;32:314.
17. Romero RL, Alfano OM, Cassano AE. Cylindrical photocatalytic reactors. Radiation absorption and scattering effects produced by suspended fine particles in an annular space. *Ind Eng Chem Res*. 1997;36:3094–3109.
18. Sgalari G, Camera-Roda G, Santarelli F. Discrete ordinary method in the analysis of radiative transfer in photocatalytically reacting media. *Int Commun Heat Mass Transfer*. 1998;25:651.
19. Chui EH, Raithby GD. Computation of radiant heat transfer on a non-orthogonal mesh using the finite-volume method. *Numer Heat Trans B*. 1993;23:269.
20. Pareek VK, Adesina AA. Light intensity distribution in a photocatalytic reactor using finite volume. *AIChE J*. 2004;50:1273–1288.
21. Rizzuti L. *Absorption of light energy in photoreactors*. In: Schiavello M, editor. *Photoelectrochemistry, Photocatalysis and Photoreactors*. Dordrecht, Holland: D. Reidel Publishing, 1985.
22. Roger M, Villermaux J. Modeling of light absorption in photoreactors: part 1. general formulation based on the laws of photometry. *Chem Eng J*. 1979;17:219–226.
23. Zhang Z, Anderson WA, Moo-Young M. Rigorous modeling of UV absorption by TiO_2 films in a photocatalytic reactor. *AIChE J*. 2000; 46:1461–1470.
24. Philips Lighting Company. *Specialty Catalogue*. Somerset, NJ, 1998:7. Available at: http://www.lighting.philips.com/pwc_li/main/application_areas/assets/phototheraphy/Philips_Phototherapy_Lamps_Catalogue.pdf.
25. Alfano OM, Romero RL, Cassano AE. Radiation field modeling in photoreactors—1: homogeneous media; 2. Heterogeneous media. *Chem Eng Sci*. 1986;41:421–444,1137–1153.
26. Zhang Z. Analysis of a corrugated plate photocatalytic reactor. *PhD Thesis, Univ. of Waterloo,* Waterloo, Ont. Canada, 1999.
27. Goswami DY. A review of engineering developments of aqueous phase solar photocatalytic detoxification and disinfection processes. *J. Solar Energy Eng*. 1997;119:101.
28. Curcó D, Malato S, Blanco J, Giménez J. Photocatalysis and radiation absorption in a solar plant. *Solar Energ Mater Sol Cell*. 1996; 44:199.
29. Turchi CS, Mehos MS. Solar photocatalytic detoxification of groundwater: developments in reactor design. *Chem Oxid*. 1994; 2:301.
30. Zhang Y, Crittenden JC, Hand DW, Perram DL. Destruction of organic compounds in water using supported photocatalysis. *J. Solar Energy Eng*. 1996;118:123.
31. US Precision Lens. *The Handbook of Plastic Optics*. Cincinnati, OH: U.S. Precision Lens, 1973.
32. Schröer H. *Luminous Flux and Illumination*. Berlin: Wissenschaft und Technik Verlag, 2001.
33. Zhang Z, Anderson WA, Moo-Young M. Radiation modeling of air phase corrugated plate photocatalytic reactor. *Dyn Continuous Discrete Impulsive Syst B Appl Algor* 2004;11:59–68.
34. Shang H, Zhang Z, Anderson WA. Non-uniform radiation modeling of a corrugated plate photocatalytic reactor. *AIChE J*. 2005;51: 2024–2033.
35. Zhang Z, Anderson WA, Moo-Young M. An engineering model for the scale-up and design of photocatalytic reactors. *Int J Chem Reactor Eng*. 2003;1:A57.
36. Imoberdorf GE, Irazoqui HA, Cassano AE, Alfano OM. Photocatalytic degradation of tetrachloroethylene in gas phase on TiO_2 films: a kinetic study. *Ind Eng Chem Res*. 2005;44:6075–6085.

Manuscript received Mar. 23, 2011, and revision received May 6, 2011.